

NON-INVASIVE ELECTRIC FIELD SENSOR FOR IMAGING CHARGED PARTICLE BEAMS AND PLASMAS

Robert Behary and Irina Novikova (advisor)
Department of Physics, William & Mary, Williamsburg, VA 23185

Experiments using quantum properties of atomic vapor can enhance future NASA missions and science directives. Atomic based electrometers can be used to probe electric fields where standard dipole antennas cannot be placed and be easily integrated for field research because of their low SWAP-C requirements. Our sensor is based on highly excited Rydberg atoms that have a large electric dipole moment and are therefore very sensitive to electric fields. As a proof of principle experiment we are using this sensor to do non-invasive diagnostics of an electron beam (e-beam) to reconstruct the beam position, size and current. We present two different methods of spatially resolving the electric field. One involves a fluorescence based measurement with a camera, and the other is done by spatially translating the laser beams in the Rb vapor volume. This technique allows for fine spatial resolution of the electron beam and can be further used to do measurements of low density plasmas or other applications of electric field imaging.

I. INTRODUCTION

Electric field measurements have been done in the past using dipole antenna technology. While this technology still works, dipole antennas can be damaged leading to inaccurate readings and are not continuously tunable for low frequency fields. Metrology institutes such as the National Institute of Standards and Technology (NIST) have been working to redefine measurable quantities in terms of fundamental constants and properties of atoms. The appeal of redefining measurements in this way is to have a standard that should be the same throughout the entire universe.

Over the past few years, there has been a great interest in the development and implementation for Rydberg states of atoms as electric field sensors. These are atoms with their valence electron excited to a high principle quantum number ($n \geq 20$) and have already been explored for a wide range of applications, including SI-traceable electric field standards¹, rf-field receivers²⁻⁴, THz-imaging⁵⁻⁷, magnetic field sensing^{8,9}, and thermometry of blackbody radiation¹⁰. NASA also has projects that can benefit from this technology in directives that seek to create images created by electric fields. Electric field images have direct applications in the medical field for brain imaging and cancer detection, security for baggage screenings, and spacecraft charging mitigation^{11,12}. Direct applications of the measurement of the electric field are relevant for justifying the advancement of electric field sensing technology, but this can also help improve fundamental science searches.

Our experiment utilizes a room temperature atomic vapor to do electric field measurements. Unlike the laser cooled atoms that are implemented in experiments in the International Space Station (ISS) now, atomic vapor poses more potential for SWAP-C potential due to a more compact and simplified design. Quantum optical sensors also provide a new and exciting opportunity for non-invasive diagnostic capabilities of objects where traditional sensors cannot reach.

In this report we present a proof of principle experiment of how Rydberg atoms can be used for non-invasive measurements of an electron beam (e-beam). We show how we can reconstruct the beam position, width and current with two different methods of spatially scanning the electron beam area. This development in the spatial mapping of electric field is not only useful for measuring an electron beam, but can be used in detecting the electric field produced by low-density plasmas and other spatially varying electric field distributions.

II. E-BEAM APPARATUS AND DETECTION METHOD

The setup and method of detecting the electron beam is shown in Fig. 1. An electron beam passes through a low density rubidium (Rb) vapor. The e-beam produces a spatially varying electric field. Rb atoms are excited to a Rydberg state with lasers to sense the generated electric field Fig. 1 (a). For small non-resonant dc electric fields, the Rydberg state will shift in frequency such that

$$\Delta f_{m_j}(E) \approx -\frac{1}{2}\alpha_{m_j}E^2. \quad (1)$$

Where α_{m_j} is the scalar polarizability of the different m_j sub levels of the Rydberg state and E is the scalar root-mean-squared (RMS) value of the electric field^{1,2,9,13}. We are dealing with relatively large values of electric fields for our targeted Rydberg state, so shifts to the Rydberg energy level are interpolated from a numerically solved Stark map generated by the Alkali Rydberg calculator (ARC) python package¹⁴ and the relative strengths of these shifts are shown in Fig. 1 (b). The low density Rb vapor is introduced to the beamline in the vacuum attachment shown in Fig. 1 (c). Shifts to the Rydberg energy levels are monitored either:

- With a photodiode that monitors the probe laser transmission through the Rb chamber.

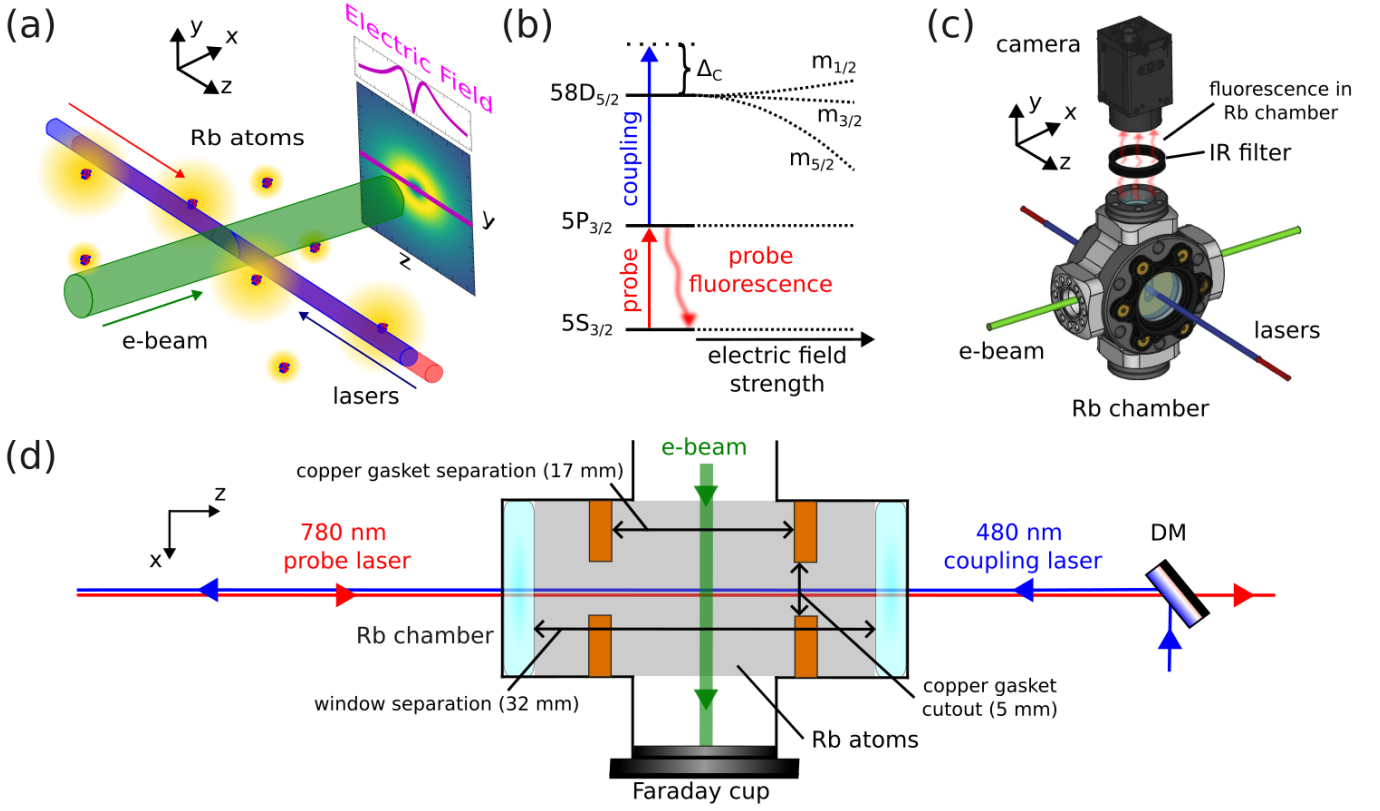


FIG. 1. Overview of experimental design. (a) A charged particle beam produces an electric field. The beam passes through a cloud of Rb atoms shown as a nucleus with electron cloud in yellow. We use lasers to excite these atoms to a Rydberg state (shown as atoms with a larger electron cloud) to probe the electric field. The beam produces a Gaussian electric field distribution described by Eq.(3). (b) Energy level diagram for Rydberg EIT. In the presence of an electric field, the m_j sublevels of the Rydberg state will shift differently based on the strength of electric field. (c) Experimental setup to capture the probe laser fluorescence in the Rb chamber with a camera. (d) Cross section of rubidium chamber on our beam line for electric field detection. Distances are marked to give a sense of scale of the setup.

- With a camera that looks into the Rb chamber when monitoring the probe laser fluorescence.

In principle both of these methods can be done at the same time, but we present the methods independently. For a sense of scale of the Rb chamber and to provide a simplified experimental setup, a cross section is shown in Fig. 1 (d). Our chamber contains copper gaskets for the purpose of blocking parasitic fields that may build up on the windows of the chamber when the e-beam is turned on and photo-illuminated fields generated by the blue laser on the chamber windows^{13,15}.

We use a Staib Instruments filament source that emits a collimated e-beam through a pulser. The pulser can modulate the e-beam up to a speed of 1 MHz. The e-beam current is monitored by a Faraday cup. Preliminary diagnostics of the e-beam are done via impact fluorescence (IF) measurements. This more invasive procedure involves increasing the rubidium density and having a long exposure time on a camera to do a one dimensional profile of the beam. IF allows for a measurement of the e-beam width at the location of our atomic detection region.

For all-optical detection we use a coherent two-photon process called electromagnetically induced transparency (EIT)^{16–18} to excite and detect atoms in the Rydberg state. EIT is monitored by overlapping a 780 nm probe laser and 480 nm coupling laser through a vapor cell, and monitoring the probe laser absorption with a photodiode or the fluorescence with a camera^{18–21}. The two-photon EIT scheme leads to a simple experimental setup, where the overlapped lasers create a volume of atoms promoted to a highly polarized Rydberg state that is sensitive to electric fields. For our optical components the 480 nm laser is a Toptica diode laser tuned to the 58D Rydberg resonance with scalar polarizability $\alpha = 674 \text{ MHz}/(\text{V}^2/\text{cm}^2)$ for the $58D_{5/2} m_j = 5/2$ state¹⁴. To measure the EIT spectra we lock the probe laser to the $^{85}\text{Rb } 5S_{1/2} (F=3) \rightarrow 5P_{3/2} (F=2 \text{ co } 3)$ resonance and sweep the frequency of the coupling laser around the 58D Rydberg resonance. The source of rubidium is an ampule placed at the bottom of the chamber. The chamber is in a box that is heated with hot air at 55°C to increase the rubidium density with a total pressure in the beam line of $2 \times 10^{-8} \text{ Torr}$.

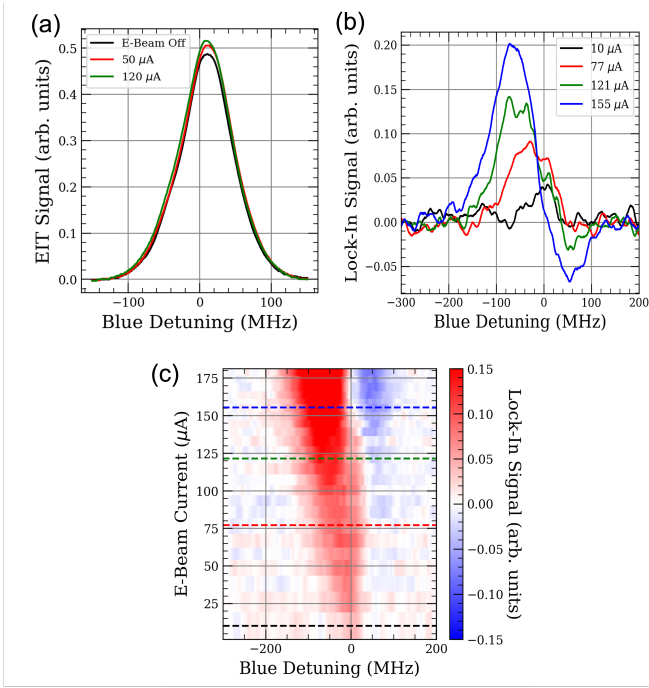


FIG. 2. An example of our detected signals and showing the need for lock-in detection on the pulsing of the e-beam. (a) Our EIT signal is broad and it is difficult to see changes to the line shape for increasing e-beam current. (b) Pulsing the e-beam we can get a lock-in signal that is more pronounced along the blue detuning axis, and the signal grows with increasing e-beam strength. (c) An example of how the lock-in signal is used to see changes against a parameter. The heat map is the strength of the lock-in signal shown in (b), and is useful for visualizing the increasing field. Dashed lines are the lock-in curves shown (b).

III. LASER TRANSLATION BASED MEASUREMENTS

This section shows work that was done for spatial measurements that lack great spatial resolution, but can be beneficial because instead of a camera, it uses a simple photodiode for measuring EIT.

To gain spatial resolution of the field within the cell, the red and blue beams are crossed at an angle $\phi \approx 7^\circ$. For the measured red beam width the length of our overlapped detection region of the red and blue laser beams is calculated to be ≈ 5 mm. While not a very fine horizontal sensitivity, this is a much smaller interaction region than the length of the cell (2 cm). The angle of overlap ϕ is limited by copper plates within the Rb chamber that mitigates charging on the glass and the broadening and strength of the EIT peak at larger angles.

Fig. 2(a) shows an example of our recorded EIT spectra due to the presence of the e-beam. To align the e-beam and the lasers, we use polarization rotation methods to align the red laser with the e-beam²², and then move the blue laser until the signal is maximized on the

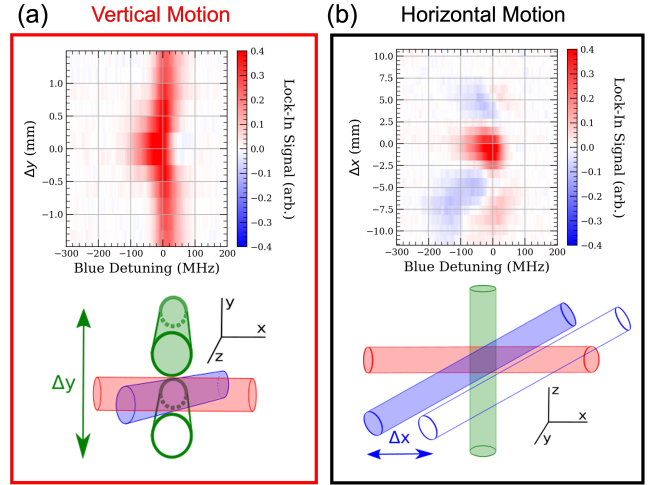


FIG. 3. Description of how the field is changed in the horizontal and vertical directions. In both plots the red cylinder is the red laser beam, the blue cylinder is the blue laser beam, and the green cylinder is the e-beam. (a) By moving the electron beam vertically with the pulser deflection coils around the crossed laser beam region we can extract a symmetric shape that is due to the presence of the electron beam. (b) By moving the blue laser horizontally with a thick glass plate that is tilted we see a large background and a large red spot that is due to the electron beam. We can't fully characterize the background, but we use PCA analysis to extract important features within the heat map.

lock-in output. As shown in the black trace, the EIT is broad due to the laser beams being at an angle. The frequency axis is calibrated with a separate EIT reference cell and the hyperfine splitting of the $58D_{5/2}$ and $58D_{3/2}$ sub-levels¹⁴. The other two traces in Fig. 2(a) show a lineshape distortion compared to the e-beam off case, but no apparent splitting of the EIT peak. Because the electric field produced by the e-beam is inhomogeneous it will only broaden the EIT peak. Having the beams crossed at an angle with a relatively small overlap region, we sense only the broadening in a particular location within the Rb chamber. The lineshape distortion is also nearly unnoticeable compared to the width of the EIT resonance, so the e-beam is pulsed at ≈ 5 kHz to perform lock-in detection.

The result of this modulation is that the lock-in amplifier can detect changes happening at that frequency in our signal and give us a resulting trace as shown in Fig. 2(b). Fig. 2(b) shows a much higher contrast signal with more easily resolvable features within the EIT lineshape detuning range. Fig. 2(c) compresses a lot of data into a single plot where the x -axis is the blue laser detuning, and the y -axis is increasing e-beam current. The heat map coloring is the resulting lock-in signal amplitude. Fig. 2(c) shows a clear trend that as the e-beam current increases, the lock-in signal amplitude and shift along the blue detuning axis increases which is indicative of increasing electric field strength.

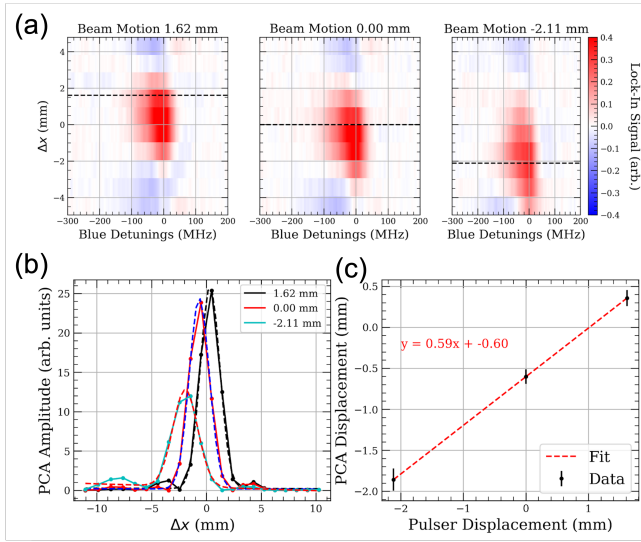


FIG. 4. Showing that the red feature in Fig. 3 is due to the presence of the electron beam. (a) Heat maps showing the horizontal motion of the blue laser beam for varying electron beam horizontal deflections. The black dashed lines show the expected centers of the electron beam from the pulser deflection calibrations. (b) PCA of the heat maps in (a). The Gaussian feature shows that there is a distinguishable feature within the heat maps. This is fit and the center is extracted for each position. (c) PCA extracted center vs. pulser displacement to show the correlated motion.

Plots shown in Fig. 2 show a dependence on the current of the e-beam, but we also want information on the spatial distribution of the electric field. To gain this information we need to raster scan the 2D plane of the laser beam path, and how this is done is shown in Fig. 3. For the vertical motion in the Rb chamber, the field is changed by moving the e-beam with the pulser deflection coils. This is not an ideal case because this has potential to change the electrostatic environment, but simplifies the optical detection apparatus as the laser beams don't have to be vertically translated. Fig. 3(a) shows the resulting heatmap of the vertical motion of the e-beam. The takeaway from Fig. 3(a) is that there is a symmetric feature in the center of the vertical position sweep that is attributable to the EIT lineshape change generated by the e-beam. This is also our higher spatial sensitivity axis, as the only limiting factor of spatial resolution is the width of the laser beams which is ≈ 0.2 mm.

The more complicated axis to interpret is the horizontal motion of the 2D raster scan. The horizontal displacement of the blue overlap region is controlled with a thick piece of glass. With the thick glass, we can horizontally translate the blue laser by a distance d and calculate approximately where the center overlap region is within the cell Δx . The relation for d and Δx is a simple geometric relation related to tilting the thick glass and are given by

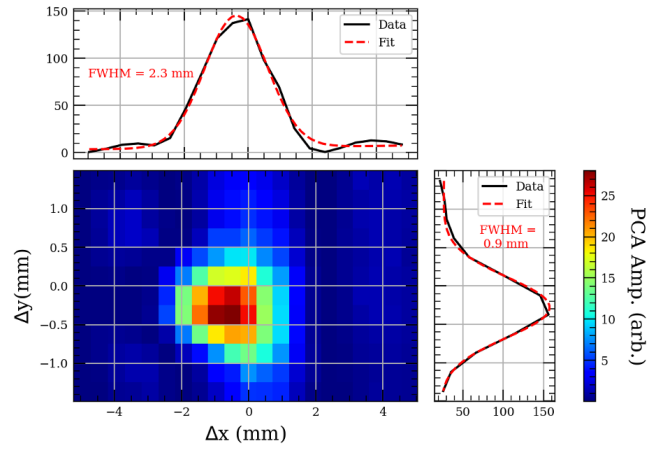


FIG. 5. 2D beam profile with widths calculated along both axes. The y amplitude is our more precise measurement axis and is in good agreement with the width obtained from fluorescence.

$$d = t[\tan\theta - \tan(\sin^{-1}[\frac{\sin\theta}{n_2}])] \cos\theta \quad (2a)$$

$$\Delta x = d/\sin\phi. \quad (2b)$$

Where t is the thickness of the thick glass 1.2 cm, θ is the angle of the thick glass, n_2 is the index of refraction of the glass 1.5, and ϕ is the angle of intersection of the red and blue laser $\approx 7^\circ$. Through this conversion, we can calculate how far within the Rb chamber we move the overlap region by rotating the thick glass. Fig. 3(b) shows the resulting heat map of the horizontal motion of the 2D raster scan. From its asymmetric shape it is apparent that there is an electric field gradient generated by the e-beam within the Rb chamber. This can be attributed to the beam pulsing some ambient charging within the metal, Rb ionization and creating some plasma, or any number of charging effects we don't have the infrastructure to mitigate with our current Rb chamber. However, there is a strong red feature that appears within the cell that is due to the e-beam itself.

To show this feature is due to the e-beam, we move it horizontally with the pulser deflection coils to see if it also moves for the same horizontal position sweep. Fig. 4 shows that this feature does move as we move the e-beam position. Fig. 4(a) is the heat map signal of the horizontal blue laser position scan where the red dot center moves along the y -axis for the different beam positions. For simplicity, we only show the horizontal scan positions around where the red feature is located. The black dashed lines show the expected e-beam positions using the fluorescence calibration data for the pulser deflection coils. While the black dashed lines do not sit in the center of the red dot feature in each heat map, the trend looks the same. To further verify this trend we use a principal component analysis (PCA) to extract a physically

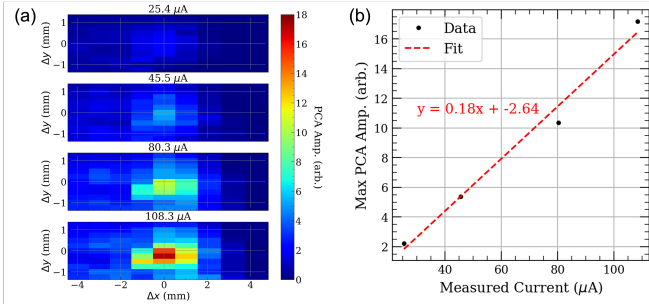


FIG. 6. Showing our attempt at calibrating the electron beam current. (a) 2D beam profiles for increasing electron beam current. The steps are not as fine as those in Fig. 5 but shows the same behavior. (b) Calibration of how measured signal can be converted to electron beam current.

relevant parameter of change. Through this analysis in Fig. 4(b), there are clear Gaussian peaks that translate along the Δx axis, and is distinctly distinguishable from the ambient background also present in each of these figures. These peaks are fit with a Gaussian, and the center of this fit is plotted vs. the horizontal motion expected from the deflection coils in Fig. 4(c). This data is fit with a line, and if the motion is truly corresponding, the slope of this line should be one, but it is 0.6. That means that this motion is not one-to-one, but it might be thrown off due to calibration mismatch of the horizontal motion of the deflection coils, or uncertainty in the horizontal detection region for our rastering method. The greater take away of this graph is that in the horizontal motion of the blue laser, we can attribute the red dot feature to the electric field of the e-beam, and can therefore do a full 2D raster scan to get a profile of the e-beam.

Combining all that we understand about the interior of the cell, we now perform a 2D raster scan and extract a beam profile shown in Fig. 5. This profile was done with a measured e-beam current of $108 \mu\text{A}$, a fixed horizontal deflection, and a vertical and horizontal rastering procedure described by Fig. 3. The Δx -axis covers a larger range and shows an asymmetry to the beam. Asymmetry may be due to spurious charging within the cell or uncertainty in the wider detection region in the horizontal direction. To extract beam parameters the axes are averaged, and fit with a Gaussian and linear background. The FWHM along the vertical Δy direction is 0.9 mm , and is in agreement with the widths of the fluorescence data that has a FWHM of $1 \text{ mm} \pm 0.1 \text{ mm}$. The FWHM along the horizontal Δx direction is a factor of two larger being 2.3 mm , but again, the detection volume in this direction is also $\approx 5 \text{ mm}$, which is much larger than the vertical direction. Despite poor resolution in the x -direction, this method shows that it can be useful to resolve fields for a 2D profile of the e-beam.

One final parameter we want to extract from the e-beam using this method is the current. While we have shown that there are spurious charges that are in our Rb chamber, we can do an empirical calibration to show that

the despite these charges, we can calibrate the readout per system as shown in Fig. 6. Fig. 6(a) shows the 2D profile of the e-beam like that in Fig. 5 for increasing currents. These profiles have less fine steps, but all we are concerned about is extracting the maximum value from these profiles. Plotting the measured current value vs. the extracted maxima from the beam profiles, we see a linear correlation between the two. While it would be more ideal to have a known background field so that the shifted signal along the detuning axis would be a more standard calibration, this shows how this method could be used at any facility to say something about the beam strength.

IV. FLUORESCENCE BASED MEASUREMENTS

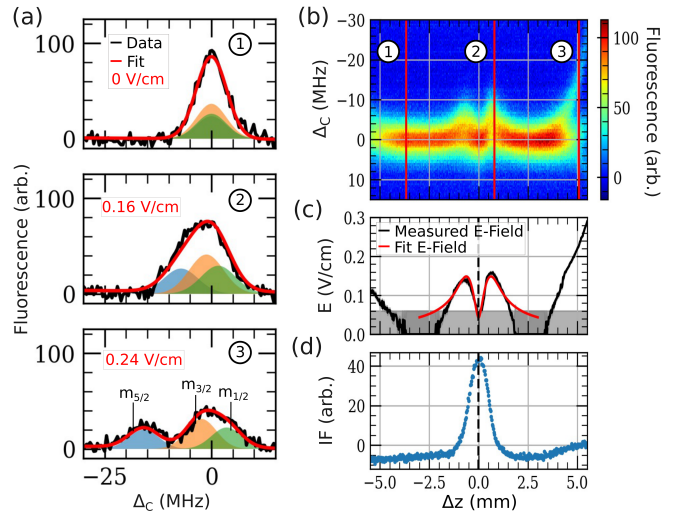


FIG. 7. Demonstration of fluorescence based measurements in the presence of e-beam. (a) The EIT spectra that constitute the heat map in (b). The spectra are fit with a sum of Gaussians to determine the electric field value shown as the shaded regions in each plot. (b) The measured spectra of the $58D_{5/2}$ Rydberg EIT peak for each position along the laser beam fluorescence. The numbers correspond to the shown single spectra in (a). (c) The reconstructed electric field value along the Rb chamber. The minimum detectable field is shown as a strip along the bottom of the plot, and error bars on the fit are shown in grey. (d) Electron beam profile obtained from IF.

This section shows work that was done for spatial measurements that is promising work that will be soon published and was done in collaboration with a group at NIST.

Rydberg fluorescence measurements are done by monitoring the $5P_{3/2}$ state decay as the coupling laser is slowly swept across the $58D$ Rydberg state. The coupling laser sweep slowly and the camera collects images at a fixed frame rate. Again, the $58D_{5/2}$ and $58D_{3/2}$ hyperfine splitting is used to calibrate the frequency axis.

Our camera is focused on the plane of the laser fluorescence within the Rb chamber. Image size is calibrated to a picture of a ruler with the same imaging system. An infrared (IR) filter that has a band pass for 780 nm light is placed in front of the lens to eliminate background and increase signal to noise for the probe laser fluorescence.

We are dealing with relatively large values of electric fields for our targeted Rydberg state, so shifts to the Rydberg energy level are interpolated from a numerically solved Stark map generated by the Alkali Rydberg calculator (ARC) python package¹⁴ and the relative strengths of these shifts are shown in Fig. 1 (b).

In Fig. 7, we show the measured spectra, and how they correspond to the presence of the electron beam. Fig. 7 (a) shows EIT spectra for different positions along the laser beam path. The number in each plot shows where they lie along the laser beam fluorescence position in Fig. 7 (b). The total EIT profile \mathcal{F} are modeled with a sum of Gaussians corresponding to the different m_j levels of the corresponding Rydberg state such that

$$\mathcal{F} = A \sum_{m_j} w_{m_j} \exp\left(\frac{-(\Delta_C - \Delta f_{m_j}(E))^2}{2\gamma_{EIT}^2}\right).$$

Where w_{m_j} are relative peak intensity values corresponding to the values of each m_j level of the Rydberg state Δ_C is the coupling laser detuning, γ_{EIT} is the linewidth of the EIT resonance measured from the fluorescence and set constant for all fits, and $\Delta f_{m_j}(E)$ is the shift to the Rydberg energy level described by the numerical calculation of the Stark map from ARC^{9,13,14}. In this fit, the only free parameters are the total amplitude of the EIT profile A and the value of electric field E .

The reconstructed electric field distribution is shown in Fig. 7 (c). For the signal to noise in our experiment, the minimum splitting is ≈ 0.5 MHz, which corresponds to a minimum field value of ≈ 0.06 V/cm. Below this value, the reconstructed electric field values are not trustworthy. The reconstructed electric field in Fig 7 (c) shows a large electric field near the edges of the fluorescence region. To help guide the eye, Fig. 7 (d) shows the IF of the e-beam to show the size and location along the fluorescence region. The e-beam is not present near the edges of the fluorescence region, but there is a semi-symmetric electric field that is centered around the e-beam center.

The reconstructed electric field curve is fit with a Gaussian electric field distribution calculated by

$$E_{e-beam} = \frac{I}{2\pi\epsilon_0 v_e r} \left(1 - e^{-\frac{r^2}{\sigma_{beam}^2}}\right). \quad (3)$$

Where σ_{beam} is the half-width at half maximum of the e-beam, ϵ_0 is the electric constant, $r = \sqrt{(z + dz)^2 + y^2}$ is the radial position away from the e-beam and dz is its displacement along the z -direction, I is the e-beam current, and v_e is the speed of the electron given by $v_e = \sqrt{\frac{2eV}{m_e}}$. For v_e , e is the electron charge, m_e is the electron mass, and V is the electron energy - 20 keV. This fit also accounts for the integrated width of the laser beam and the

y -deflection from center of the electron beam. The free parameters in this fit are the e-beam size σ_{beam} , e-beam current I , and the z and y -displacement of the electron and laser beams respectively. We fit the reconstructed electric field with this function to extract the parameters of the e-beam.

For the data presented in this paper, the FWHM is fixed and monitored with the IF measurements. We find good agreement with the two methods to measure electron beam width where the IF has a value of 1.07 ± 0.06 mm the reconstructed with from the electric field has a value of 1.1 ± 0.3 mm. The value of the width is measured from repeated measurements with a fixed Faraday cup current of $35 \mu\text{A}$.

Further diagnostics of the e-beam position and current are shown in Fig. 8. Fig. 8 (b) shows the correlation between the center of the impact-induced e-beam fluorescence in the chamber and the beam center found through the reconstructed electric field fit. We find that these values are highly correlated through a linear fit that shows both methods yield nearly the same center position.

A characterization of the current is shown in Fig. 8 (d). Here, the dependence of current and the measured current on the Faraday cup are not correlated linearly. This is most likely due to the influence of the large parasitic field within the Rb chamber that is visible in Fig. 7 (d) when the beam is not on inside the chamber. We also observed that the strength of the beam can cause the charging within the cell to change. Our simple fit model also doesn't take into account the direction of the electric field, and how this will influence the shifts of the different m_j levels of the Rydberg state. The beam current is also difficult to measure because we do not have an in-situ tool to measure the current at the location of the Rydberg measurement. Also for different current values of the e-beam, it can slightly distort the beam shape as shown in the e-beam fluorescence measurements shown in Fig. 8 (c). For more precise control of the background field, and information about the direction of the electric field produced by the electron beam, a more advanced Rb chamber with capacitor plates needs to be constructed.

V. CONCLUSION

We have shown a successful application of Rydberg atom based electric field sensors for a novel purpose of measuring a charged particle beam. Currently we are working on ways to improve our Rb chamber to account for directions of electric field, and searching for ways to mitigate the parasitic background charge we are sensitive two in both methods of our spatial field distribution measurements. This is a big step towards non-invasive measurements of charged particle beams, but we are also constructing a plasma chamber to perform these same types of measurements in plasma. All together this work has potential for being useful in expanding basic science research and understanding things such as stellar plasma

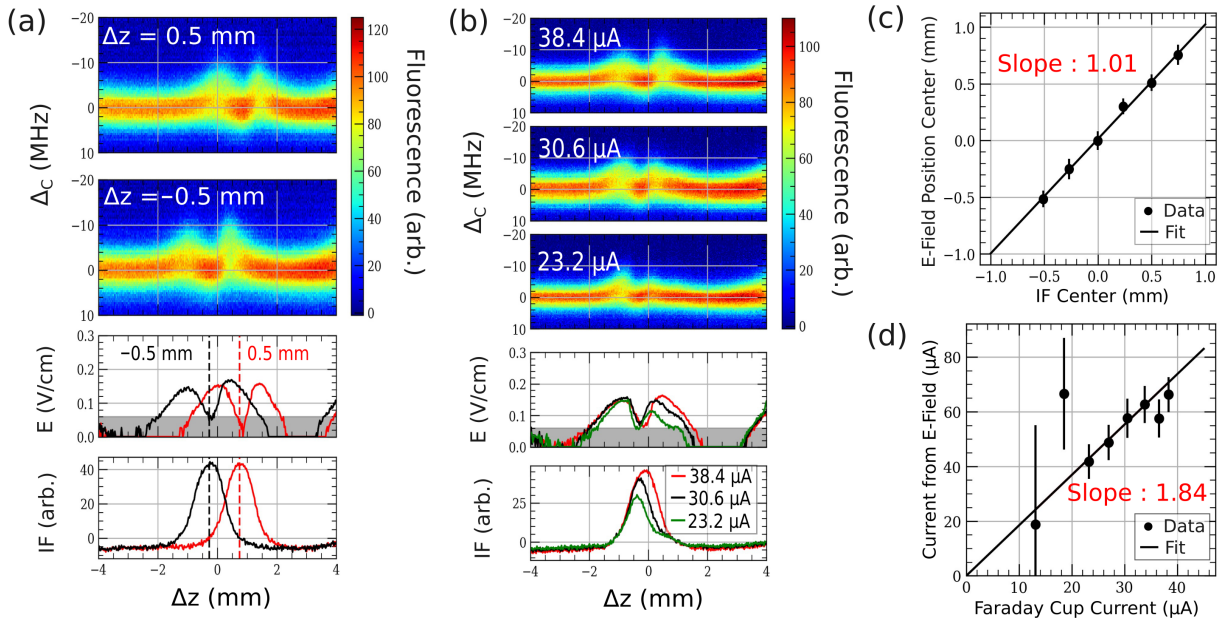


FIG. 8. E-beam diagnostics for position and current. (a) and (b) are the same style of plots shown in Fig. 7 (b)-(d). (a) Heat maps for two different e-beam positions in the cell. The dashed lines in the plots show the beam center. (b) Plots of heat maps for increasing e-beam current. Current values recorded from the Faraday cup. (c) Diagnostic of e-beam position in the Rb chamber. The Rydberg position matches well with the center of the impact-induced fluorescence. Error bars are fit error estimation plus the width of a single pixel on the camera. (d) Fit of recovered Rydberg current vs. Faraday cup current. Error bars are fit error estimation plus the width of the minimum detectable field.

and charged particle tracks.

VI. ACKNOWLEDGMENTS

This work is supported by the Virginia Space Grant Consortium (VSGC), Department of Energy, Depart-

ment of Defense, Defense Advanced Research Projects Agency and LDRD. We would like to acknowledge collaborators from NIST Boulder for their work and help on the fluorescence based Rydberg measurements, and Kevin Su (W&M) for his preliminary work on the crossed beam geometry measurements.

-
- [1] Christopher L. Holloway, Matt T. Simons, Joshua A. Gordon, Andrew Dienstfrey, David A. Anderson, and Georg Raithel. Electric field metrology for si traceability: Systematic measurement uncertainties in electromagnetically induced transparency in atomic vapor. *Journal of Applied Physics*, 121(23):233106, 2017.
- [2] Noah Schlossberger, Nikunj Kumar Prajapati, Samuel Berweger, Andrew P. Rotunno, Alexandra B. Artusio-Glimpse, Matthew T. Simons, Abrar A. Sheikh, Eric B. Norrgard, Stephen P. Eckel, and Christopher L. Holloway. Rydberg states of alkali atoms in atomic vapour as si-traceable field probes and communications receivers. *Nature Reviews Physics*, 6(10):606–620, 2024.
- [3] Peter K. Elgee, Joshua C. Hill, Kermit-James E. LeBlanc, Gabriel D. Ko, Paul D. Kunz, David H. Meyer, and Kevin C. Cox. Satellite radio detection via dual-microwave rydberg spectroscopy. *Applied Physics Letters*, 123(8):084001, 08 2023.
- [4] Charles T. Fancher, David R. Scherer, Marc C. St. John, and Bonnie L. Schmittberger Marlow. Rydberg atom electric field sensors for communications and sensing. *IEEE Transactions on Quantum Engineering*, 2:1–13, 2021.
- [5] Matt T. Simons, Joshua A. Gordon, and Christopher L. Holloway. Fiber-coupled vapor cell for a portable rydberg atom-based radio frequency electric field sensor. *Appl. Opt.*, 57(22):6456–6460, Aug 2018.
- [6] Lucy A Downes, Lara Torralbo-Campo, and Kevin J Weatherill. A practical guide to terahertz imaging using thermal atomic vapour. *New Journal of Physics*, 25(3):035002, mar 2023.
- [7] Lucy A. Downes, Andrew R. MacKellar, Daniel J. Whiting, Cyril Bourgenot, Charles S. Adams, and Kevin J. Weatherill. Full-field terahertz imaging at kilohertz frame rates using atomic vapor. *Phys. Rev. X*, 10:011027, Feb 2020.
- [8] Noah Schlossberger, Andrew P. Rotunno, Alexandra B. Artusio-Glimpse, Nikunj Kumar Prajapati, Samuel Berweger, Dangka Shylla, Matthew T. Simons, and Christopher L. Holloway. Zeeman-resolved autler-townes

- splitting in rydberg atoms with tunable resonances and a single transition dipole moment. *Phys. Rev. A*, 109:L021702, Feb 2024.
- [9] Noah Schlossberger, Tate McDonald, Kevin Su, Rajavardhan Talashila, Robert Behary, Charles L. Patrick, Daniel Hammerland, Eugeniy E. Mikhailov, Seth Aubin, Irina Novikova, Christopher L. Holloway, and Nikunj Kumar Prajapati. Two-dimensional imaging of electromagnetic fields via light sheet fluorescence imaging with rydberg atoms, 2024.
- [10] Noah Schlossberger, Andrew P. Rotunno, Stephen P. Eckel, Eric B. Norrgard, Dixith Manchaiah, Nikunj Kumar Prajapati, Alexandra B. Artusio-Glimpse, Samuel Berweger, Matthew T. Simons, Dangka Shylla, William J. Watterson, Charles Patrick, Adil Meraki, Rajavardhan Talashila, Amanda Younes, David S. La Mantia, and Christopher L. Holloway. Primary quantum thermometry of mm-wave blackbody radiation via induced state transfer in rydberg states of cold atoms. *Phys. Rev. Res.*, 7:L012020, Jan 2025.
- [11] Ed Generazio. Electric potential and electric field imaging with dynamic applications: 2017 research award innovation. In *ASNT Research Symposium*, number NF1676L-26141, 2017.
- [12] E. I. Lin and M. dePayrebrune. An educational multimedia presentation on the introduction to spacecraft charging. 2004.
- [13] Link Patrick, Noah Schlossberger, Daniel F. Hammerland, Nikunj Kumar Prajapati, Tate McDonald, Samuel Berweger, Rajavardhan Talashila, Alexandra B. Artusio-Glimpse, and Christopher L. Holloway. Imaging of induced surface charge distribution effects in glass vapor cells used for rydberg atom-based sensors, 2025.
- [14] N. Šibalić, J.D. Pritchard, C.S. Adams, and K.J. Weatherill. Arc: An open-source library for calculating properties of alkali rydberg atoms. *Computer Physics Communications*, 220:319–331, 2017.
- [15] L. Ma, E. Paradis, and G. Raithel. Dc electric fields in electrode-free glass vapor cell by photoillumination. *Opt. Express*, 28(3):3676–3685, Feb 2020.
- [16] Marlan O. Scully and M. Suhail Zubairy. *Quantum Optics*. Cambridge University Press, 2001.
- [17] James Keaveney, Armen Sargsyan, David Sarkisyan, Aram Papoyan, and Charles S Adams. Active narrowband filtering, line narrowing and gain using ladder electromagnetically induced transparency in an optically thick atomic vapour. *Journal of Physics B: Atomic, Molecular and Optical Physics*, 47(7):075002, mar 2014.
- [18] Lu Ma. *Electromagnetic Field Sensing with Rydberg Atoms in Vapor Cells*. Ph.D. thesis, University of Michigan, 2021.
- [19] Hsuan-Jui Su, Jia-You Liou, I-Chun Lin, and Yi-Hsin Chen. Optimizing the rydberg eit spectrum in a thermal vapor. *Opt. Express*, 30(2):1499–1510, Jan 2022.
- [20] Andrew P. Rotunno, Amy K. Robinson, Nikunj Kumar Prajapati, Samuel Berweger, Matthew T. Simons, Alexandra B. Artusio-Glimpse, and Christopher L. Holloway. Inverse transform sampling for efficient Doppler-averaged spectroscopy simulations. *AIP Advances*, 13(7):075218, 07 2023.
- [21] Kevin Su, Rob Behary, Seth Aubin, Eugeniy E. Mikhailov, and Irina Novikova. Two-photon rydberg eit resonances in non-collinear beam configurations. *J. Opt. Soc. Am. B*, 42(4):757–762, Apr 2025.
- [22] Nicolas DeStefano, Saeed Pegahan, Aneesh Ramaswamy, Seth Aubin, T. Averett, Alexandre Camsonne, Svetlana Malinovskaya, Eugeniy E. Mikhailov, Gunn Park, Shukui Zhang, and Irina Novikova. Electron beam characterization via quantum coherent optical magnetometry. *Applied Physics Letters*, 125(26):264001, 12 2024.